Research Article | Vol. 12, No. 10 / 1 Oct 2021 / Biomedical Optics Express 6341

Biomedical Optics EXPRESS

Estimation of scleral mechanical properties from air-puff optical coherence tomography

DAVID BRONTE-CIRIZA,[1,2,6,7] JUDITH S. BIRKENFELD,[1,6,8] ANDRÉS DE LA HOZ,[1] ANDREA CURATOLO,[1,3,4] JAMES A. GERMANN,[1] LUPE VILLEGAS,[1] ALEJANDRA VAREA,[1] EDUARDO MARTÍNEZ-ENRÍQUEZ,[1] AND SUSANA MARCOS[1,5]

[1] *Instituto de Óptica "Daza de Valdés", Consejo Superior de Investigaciones Científicas (IO-CSIC), Madrid, Spain*
[2] *CNR – IPCF, Istituto per i Processi Chimico-Fisici, Messina, Italy*
[3] *International Centre for Translational Eye Research, Warsaw, Poland*
[4] *Institute of Physical Chemistry, Polish Academy of Sciences, Warsaw, Poland*
[5] *Center for Visual Science, The Institute of Optics, Flaum Eye Institute, University of Rochester, NY 14642, USA*
[6] *Co-first authors*
[7] *brontecir@ipcf.cnr.it*
[8] *j.birkenfeld@io.cfmac.csic.es*

Abstract: We introduce a method to estimate the biomechanical properties of the porcine sclera in intact eye globes *ex vivo*, using optical coherence tomography that is coupled with an air-puff excitation source, and inverse optimization techniques based on finite element modeling. Air-puff induced tissue deformation was determined at seven different locations on the ocular globe, and the maximum apex deformation, the deformation velocity, and the arc-length during deformation were quantified. In the sclera, the experimental maximum deformation amplitude and the corresponding arc length were dependent on the location of air-puff excitation. The normalized temporal deformation profile of the sclera was distinct from that in the cornea, but similar in all tested scleral locations, suggesting that this profile is independent of variations in scleral thickness. Inverse optimization techniques showed that the estimated scleral elastic modulus ranged from 1.84 ± 0.30 MPa (equatorial inferior) to 6.04 ± 2.11 MPa (equatorial temporal). The use of scleral air-puff imaging holds promise for non-invasively investigating the structural changes in the sclera associated with myopia and glaucoma, and for monitoring potential modulation of scleral stiffness in disease or treatment.

© 2021 Optical Society of America under the terms of the OSA Open Access Publishing Agreement

1. Introduction

Current theories on the refractive error development of the human eye acknowledge the pivotal role of the sclera, the opaque part of the ocular globe, in myopia progression [1]. Myopia is the most common refractive error, affecting about 22% of the world population [2]. This percentage has been increasing over the last years, reaching a 90% prevalence rate in some Asian populations [3].

Myopia is the result of a mismatch between the focal length of the ocular components and the axial length of the eye, by which images are focused in front of the retina, rather than on the retinal photoreceptor layer. Excessive axial growth is responsible for 95% of myopia cases. It has been suggested that the ocular components (cornea and crystalline lens) also experience changes in myopes, although to a lesser degree. Myopic patients exhibit, for example, a thinner crystalline lens and lower lens power compared to emmetropic subjects [4–6], presumably aiming to compensate for the axial elongation [7]. There is also *in vivo* evidence in humans of morphometry differences between the anterior sclera of myopes and emmetropes [8,9].

#437981 https://doi.org/10.1364/BOE.437981
Journal © 2021 Received 16 Jul 2021; revised 15 Aug 2021; accepted 15 Aug 2021; published 17 Sep 2021

Biomedical Optics EXPRESS

The sclera has the ultimate impact on restraint or facilitation of eye growth, and thus possibly playing a role during myopia development [10]. The sclera is a connective tissue with its extracellular matrix being mainly comprised of bundles of collagen fibers [11,12]. In highly myopic eyes, the posterior pole of the sclera has been found to be thinner than in emmetropic eyes [13]. Scleral thinning has been associated with a decreased collagen fibril diameter and a narrowing of collagen fiber bundles [14]. In addition, studies in animal models (tree shrew, for example) have shown that this tissue loss involves both an accelerated scleral matrix degradation and a slowed production of new extracellular matrix [15]. These studies have also shown an alteration of the scleral biomechanical properties in the equatorial and posterior regions, which supports the hypothesis that induced changes in the axial length of the mammalian eye may be mediated by changes in the creep properties of the sclera [16].

There is an emerging attempt at strengthening the sclera to prevent myopia development by means of localized collagen cross-linking (scleral cross-linking, SXL), in a way similar to corneal cross-linking (CXL). Photo-chemical CXL uses UV light and a photosensitizer (Riboflavin) to promote the formation of inter-fibrillar chemical covalent bonds [17]. Other emerging CXL procedures use green light for irradiation and Rose Bengal as a photosensitizer, with some advantages regarding penetration and duration of the procedure in both *ex vivo* and *in vivo* in rabbits [18–22]. Experimentally, SXL has been applied recently *ex vivo* [23] and *in vivo* [24–27], successfully reducing myopia progression in both rabbits [23–26] and guinea pigs [27]. It was concluded that SXL did not prevent the reduction of the number of collagen fiber bundles; however, the fiber bundles appeared denser and more regularly distributed [27]. A number of studies have found that the cross-linked sclera presents an increase in stiffness, determined by dynamic shear rheology tests [23,25] and by stress-strain tests [26]. It is also recognized that ocular biomechanics (corneal and scleral) play a fundamental role in glaucoma management, given their influence on the intraocular pressure (IOP) [28,29].

The need for non-invasive quantification of ocular mechanical properties has been recognized before, for example, for diagnostics of diseases where corneal biomechanics is compromised (i.e., keratoconus) or for surgical planning of treatments that rely on the modulation of the corneal response. *Ex vivo* measurements keeping the eye globe intact are not only an integral step towards this goal, but they have also proven less variable than mechanical measurements performed on corneal or scleral strips, generally by extensiometry [26,30–32]. As for the cornea, scleral mechanical properties are measured more reliably using techniques that keep the eye globe intact [33]. Inflations tests [34,35] preserve the shape of the ocular globe but vary the IOP by means of an inserted cannula that is connected to an external water column, generally increasing it well above physiological values. Promising methods for the measurement of ocular mechanical properties *in vivo* include wave-based Optical Coherence Elastography (OCE) [36–38] and Brillouin microscopy [39]. Wave-based OCE investigates ocular biomechanics by using the propagation of mechanical waves to visualize the mechanical contrast of soft tissue. OCE has been recently applied to the scleral region for the measurement of the shear modulus *ex vivo* [40] and *in vivo* [41]. Brillouin microscopy, another optical method based on a materiaĺs Brillouin light scattering, offers the possibility to create a spatially resolved stiffness map of a material. It has been used extensively on the cornea, for example in keratoconus patients [42], and has been recently investigated for the use in the sclera [39,42,43].

Air-puff deformation imaging (APDI) techniques, applied to the cornea, have been presented in recent years not only as accurate tonometers, but as a method to reveal information highlighting normal and pathological corneal response to a non-contact mechanical excitation [44]. The inclusion of parameters obtained with the same imaging system (such as corneal thickness and stiffness indices [45,46]) allows for corrected estimates of IOP, compared to standard Goldman tonometry, which holds important assumptions regarding corneal thickness and corneal mechanical properties (on which corneal applanation is also dependent). One advantage of APDI

Biomedical Optics EXPRESS

is not only that it has received clearance from the U.S. Food and Drug Administration and that it has been successfully implemented into clinical practice, but that the deformation behavior could give valuable information about both, the Youngś modulus and the Shear modulus, while for OCE, the biomechanical information are based on the estimation of the shear modulus only [47].

APDI systems include commercial devices such as the Oculus Corvis ST (Wetzlar, Germany), which is based on Scheimpflug imaging. Here, the horizontal meridian of the cornea is imaged while the cornea is excited with an air-puff, a method that is used routinely in the clinic [48]. In recent years, air-puff excitation units have been coupled to customized, laboratory-based Optical Coherence Tomography (OCT) systems, monitoring corneal apex deformation [49–51], and corneal deformation in one [52] and two [53] meridians. In these systems, multiple deformation parameters are obtained from the spatial-temporal corneal surface deformation [54–56]. Reconstruction of the inherent mechanical properties of corneal tissue from corneal deformation have been achieved through Finite Element Modelling (FEM) inverse optimization techniques, allowing isolation of the tissue mechanical properties from other factors [57–61]. While existing air-puff deformation methods aim at evaluating the cornea, it is recognized that the scleral mechanical properties affect the corneal deformation response to an air-puff. In particular, it has been found that corneal deformation is smaller with increasing scleral stiffness [62].

While air-puff deformation imaging and, to a lesser extent, FEM-based biomechanical reconstruction techniques, have been applied to the cornea, a natural extension of these techniques is air-puff scleral deformation imaging, where the air-puff impinges directly on scleral tissue. It is likely that the specific software in commercial instruments does not allow capturing data in tissue (and shape) other than the cornea, given the different geometry and scattering properties. However, OCT imaging can adapt to any shape thanks to its scanning flexibility and dedicated control and analysis software, allowing customized processing.

In this study, we applied a custom-built high-speed SSOCT system coupled with an air-puff excitation device coaxially aligned to the OCT system [53] on different predetermined locations of the sclera of *ex vivo* porcine eyes. Given the higher stiffness of the sclera compared to the cornea in porcine eyes [63,64], a reduced deformation in comparison to the cornea is expected. However, by controlling the air-puff unit piston speed, we can tailor the air-puff pressure to suit the stiffer sclera. On the other hand, the sclera is thinner than the cornea in most of the regions [65], which could contribute to a larger deformation.

The acquired scleral air-puff deformation data were used as input to FEM-based inverse algorithms to reconstruct scleral biomechanical properties. Application of this technique *in vivo* holds potential to monitor the progression of myopia or identify patients at risk of developing myopia or other diseases where scleral biomechanics is involved (for example glaucoma), [66] and to track the efficacy of emerging myopia treatments such as scleral cross-linking.

2. Methods

2.1. Swept source optical coherence tomography system

All images were acquired using a custom-developed SSOCT system described in [53]. The light source consists of a MEMS-based vertical cavity surface emitting laser swept-source (SL132120, Thorlabs, USA), centered at 1300 nm. The SSOCT system uses a Mach-Zender interferometer configuration and a dual balanced photodetector (PDB480C-AC, Thorlabs, USA). To attain a large depth of field and large transverse field of view suitable for sclera deformation imaging, the sample arm was designed with a 2” aperture f-theta telecentric scan lens (LSM05, Thorlabs, USA), with a 110 mm effective focal length that allows the customized air-puff unit to be inserted between the lens and the eye (Fig. 1). The system uses 3 mm-aperture low coil impedance galvanometric scanning mirrors (Saturn 1B, ScannerMAX, Pangolin, USA) for ultrafast transverse scanning, which is critical to capture deformation events that last only tens of milliseconds. An advantage

Biomedical Optics EXPRESS

of the system is that different scanning patterns can be implemented, for example a cross-scan that monitors deformation on two orthogonal axes [61,67].

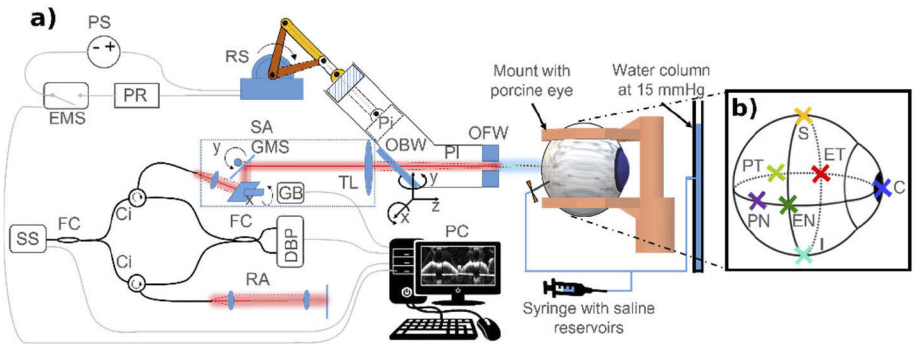

Fig. 1. a) *Ex-vivo* porcine eye positioned in the eye holder and mounted in front of the air-puff outlet and the SSOCT system (Adapted from [53]). PS: power supply, EMS: voltage-controlled switch, PR: power resistor, RS: rotary solenoid, Pi: piston, Pl: plenum chamber, OBW: optical back window, OFW: optical front window; SS: swept laser source, FC: fiber couplers, Ci: circulators, DBP: dual balanced photodetector, RA: reference arm, SA: sample arm, GMS: galvanometer mirror system, GB: galvanometer digital signal processing board, TL: telecentric f-theta lens. PC: controlling computer. The intraocular pressure of the eye was held constant at 15mmHg by means of an IOP control system that connected a syringe filled with saline solution to the eye globe (via the optic nerve) and a water column. b) All locations of air-puff excitation, C: central cornea, EN, ET: equatorial nasal and temporal locations respectively, I: inferior location, PN, PT: posterior nasal and posterior temporal location, respectively, S: superior location.

As a result, our system has an axial rate of 200 kHz, an axial resolution of 16 µm, a depth of field of 5.15 mm, a large transverse field of view of 15 mm on both orthogonal axes, and an ultra-fast transverse scanning pattern repetition frequency of 1 kHz.

2.2. Air-puff excitation source

Scleral deformation (and, for comparison, corneal deformation) was induced by a repurposed industry-standard, non-contact tonometer air-puff unit (Nidek Co., Japan). The unit has a rotary solenoid-driven, piston-based air-puff module which is coupled to the SSOCT system via an optical window at the back of the plenum chamber so that it could be mounted in front of the objective lens of the OCT system, coaxially aligned to the OCT scanning beam. With the aim of reducing nozzle wall shadowing in the OCT image, the optical window at the front of the air-puff unit was made of transparent methacrylate (with a 2.4 mm wide hole in the middle), see Fig. 1. For the current study, we set the voltage controlling the piston speed to 48 V and consequently increase the pressure by a factor of 1.14 with respect to prior studies in cornea [67]. The maximum apical pressure of the air-puff is 15.36 kPa, the duration of the full width at half maximum (FWHM) is 11.4 ms and the impact diameter at FWHM is 3.49 ± 0.07 mm.

2.3. Experimental set-up and protocol

Porcine eyes: Five freshly enucleated porcine eyes were obtained from a local slaughterhouse (Justiniano Gutíerrez S.L, Valladolid) and kept in a refrigerator at 4°C. All measurements were performed within 48 hours post-mortem. The ocular fat was removed before the measurement. A wet chamber with cotton soaked in a physiological saline solution (sodium chloride 0.9%) was used to maintain humidity during measurements.

Biomedical Optics EXPRESS

3D printed mount: A customized mount was designed with the purpose of holding the eye globes while allowing the air-puff to be applied in different scleral locations, and in the cornea for comparison (see Fig. 1(a)). The concave-convex geometry of the mount was designed to accommodate porcine globes, with dimensions obtained from the literature [49]. The superior part of the holder can be moved vertically to simplify the process of setting the eye in the desired location, before fixing it using a small screw.

Experimental protocol: The eyes were fixed in the customized holder and connected to the IOP control system with a needle through the optical nerve. The needle was not taken out until finishing all the measurements, assuring that the IOP remains constant during the experiments. The IOP was set to 15 mmHg. The eye was then positioned so that one of the predetermined locations (see Fig. 1) would face the OCT scanning beam/air-puff nozzle. The apex of the selected ocular location was then centered with the OCT's optical axis, using real time OCT image preview on cross-axes scans. For convenience, we define the most anterior point of the location that was to be scanned as the local "scleral apex".

Measurements were collected over two orthogonal axes, each of which was 15 mm long. A complete measurement consisted of a total of 100 cross-axes scans, with each axis sampled by 64 A-scans. The total acquisition time of a complete data set was 100 ms (one cross-axes scan per ms). The seven locations studied consisted of the corneal apex (C), as a control measurement, and six other locations over the sclera. In the equatorial plane of the sclera, there are the nasal (EN), temporal (ET), inferior (I) and superior (S) sclera, all located 10 mm from the limbus. The posterior nasal (PN) and the posterior temporal (PT), located at 13 mm from the limbus in each side of the eye (approx. 20 deg posteriorly from the equator), were also measured.

After a set of three measurements for each location, the eye position was carefully changed to the next location and the eye globe was moisturized with saline solution.

2.4. Finite element analysis

Finite element model simulation: A finite element model of the eye globe was built using ANSYS Workbench (ANSYS Inc, U.S.). The ocular globe was modelled as a three-dimensional, rotationally symmetric solid to reduce computational load. The dimensions used for the model were obtained from the literature [65,68]. The scleral thickness profile was considered not uniform, with the sclera being at its thinnest close to the equatorial plane, and at its thickest near the limbus and area closer to the optical nerve (~ 1 mm). The change in thickness in the geometry can be seen in Fig. 2(b). The model considers two solids (the cornea and the sclera) with a uniform material definition for each, as defined below in Eq. (1), and a boundary region representing the conditions imposed by the experiment (a holder fixing the sclera in place), see Fig. 2 (a). The interior of the ocular globe was meshed with HSFLD242 hydrostatic fluid elements, with a pressure of 15 mmHg (corresponding to the intraocular pressure in the experimental setup) applied to the central node of the fluid element mesh. The air-puff load was applied as a spatial- and time- varying pressure, using the spatial and temporal profiles obtained from measuring the air-puff over time [67].

Material models: The cornea and sclera are known to exhibit non-linear elastic stress-strain behavior due to their microstructure. In order to model this behavior, a hyper-elastic Yeoh material model with 2 parameters was used.

The Yeoh 2-parameter model is defined by:

$$W = C_{10}(I_1 - 3) + C_{20}(I_1 - 3)^2, \tag{1}$$

where W is the strain energy density function, I_1 is the first invariant of the Cauchy-Green deformation tensor, and C_{10} and C_{20} are the model parameters, retrieved experimentally from stress-strain behavior. In this model, the exponential term gives increased weight to the C_{20}

Biomedical Optics EXPRESS

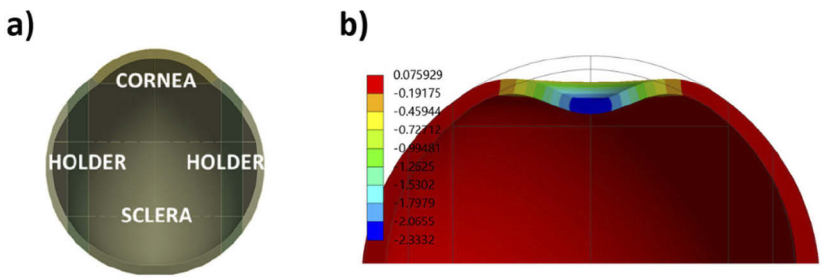

Fig. 2. Geometry used in the FEM simulations and simulation of the spatial deformation at location I during the optimization process. a) The model considers different materials of the eye globe (cornea and sclera) as well as surfaces to represent the eye holder. The holder area is assigned as a fixed support. Scleral and corneal thicknesses are selected according to existing values in the current literature [65,68], with the sclera being thinner in the equatorial-anterior region and thicker towards the posterior region. b) Spatial deformation of the sclera at the inferior part of the eye (I). The central point represents the apex displacement used for the optimization process.

parameter at higher strains and the C_{10} parameter at lower strains, which means the relative values of the parameters could be used as an indication of the material's non-linearity.

Optimization: An optimization process was constructed in Matlab (MathWorks, US) to retrieve the scleral and corneal material properties from the air-puff results. A function was built to execute ANSYS, evaluate the finite element model for a set of material parameters, retrieve the temporal profile (displacement of the central node over time), and compare the results to the corresponding experimental measurements of apex displacement. For the two-parameter Yeoh model, the 'fminsearch' function was used, and the optimization minimized the difference between the experimental and simulated apex displacements from t=0 until the time of maximum deformation. Once the two parameters were obtained, the equivalent secant Young modulus at 9% strain was computed from the stress-strain curves.

2.5. Data analysis

Data processing: The OCT images were obtained after standard image generation from wavenumber resampled spectra [69], using routines written in Matlab [67]. The optical path difference in the center of the image due to the difference in the refractive index of the 5 mm-thick methacrylate window and the air-puff unit outlet was corrected using piece-wise registration routines written in ImageJ [70].

Surface detection: A customized Matlab routine detected the ocular surfaces of the acquired deformation images. The surface detection approach involved the following steps: 1) detection of the central point of the surface, 2) sequential scanning of the image in the transverse direction identifying pixels that satisfy two conditions: proximity to the previously identified surface points, and continuity of pixel intensity (along the depth axis z, towards the inside of the eye) for at least three consecutive pixels above a predetermined intensity threshold (the threshold decreases with the distance to the apex). The segmented points were then fitted to a 9th order polynomial to obtain a continuous interpolation of the data. The segmentation process was fully automated and applied to all images of the deformation event.

Figure 3 shows two examples of surface detection at both resting position (red line) and at maximum deformation (blue line) in (a) the cornea and (b) the superior sclera (location 4).

Quantification of deformation parameters: We analyzed the following parameters for all scleral locations, and for the cornea for comparison: (1) Maximum apex deformation, defined as the highest relative distance between the apex at resting position and during air-puff excitation.

Biomedical Optics EXPRESS

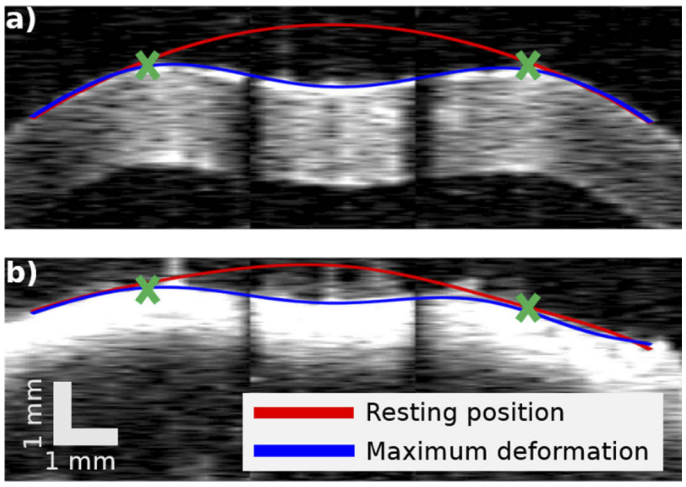

Fig. 3. Example of OCT air-puff deformation images, along with the segmented surfaces at resting position (red line) and maximum deformation (blue line) for the cornea (a) and the superior sclera (b). The green crosses, positioned at 2.8 mm (horizontally) from the apex, mark the start and ending point of the arc length measurement. The scale bar represents 1 mm in air.

(2) The temporal profile of the apex displacement and its displacement velocity (derivative of the displacement over time); (3) The arc length, defined as the length of the segmented anterior surface between two fixed symmetric locations separated 2.8 mm from the center in the horizontal axis (indicated as the detected surfaces in between the two green crosses in Fig. 3). The range of 5.6 mm was selected as a compromise between the extent of the lateral deformation and quality of segmentation (the segmentation gets worse in the periphery). The arc length was analyzed relative to that of the resting (initial) position as a function of time, whereby a relative decrease in arc length is interpreted as a compression of the material, while a relative increase is considered an extension.

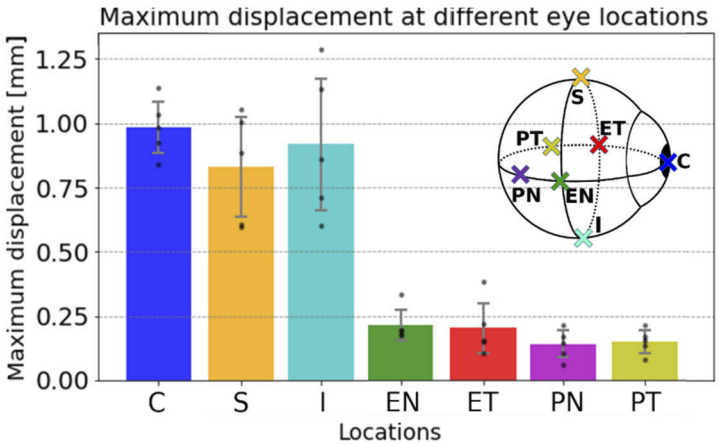

Fig. 4. Bar graph shows the average of all measured maximum deformation at all locations at the defined apex (for all eye globes). Each point corresponds to the average of the three measurements repeated at each eye. The colors correspond to the colors used in the shown icon, and the abbreviations correspond to the ones described in Fig. 1(a).

Biomedical Optics EXPRESS

Statistical Analysis: SPSS 25.0 for Windows (IBM SPSS, Chicago, Illinois, USA) was used for statistical analysis. For the experimental data, a test-retest reliability analysis was performed to indicate the degree of agreement of the three repeated measurements for each eye and each location. Pairwise comparisons between the maximum deformations at different locations (section 3.1) were done using the Friedman test (non-parametric) and the GLM Repeated Measures procedure (ANOVA, parametric, based on estimated marginal means, and using Bonferroni adjustment for multiple comparisons). To define the starting point of the investigated ingoing deformation phase (section 3.2), an ANOVA test on all locations between 0 ms and 15 ms (post-hoc test, Dunnet´s test, reference C) was executed. A quadratic regression model was used to analyze the differences in the Standard Time Profiles (STPs) during ingoing deformation phase (section 3.2, Fig. 5 (b)).

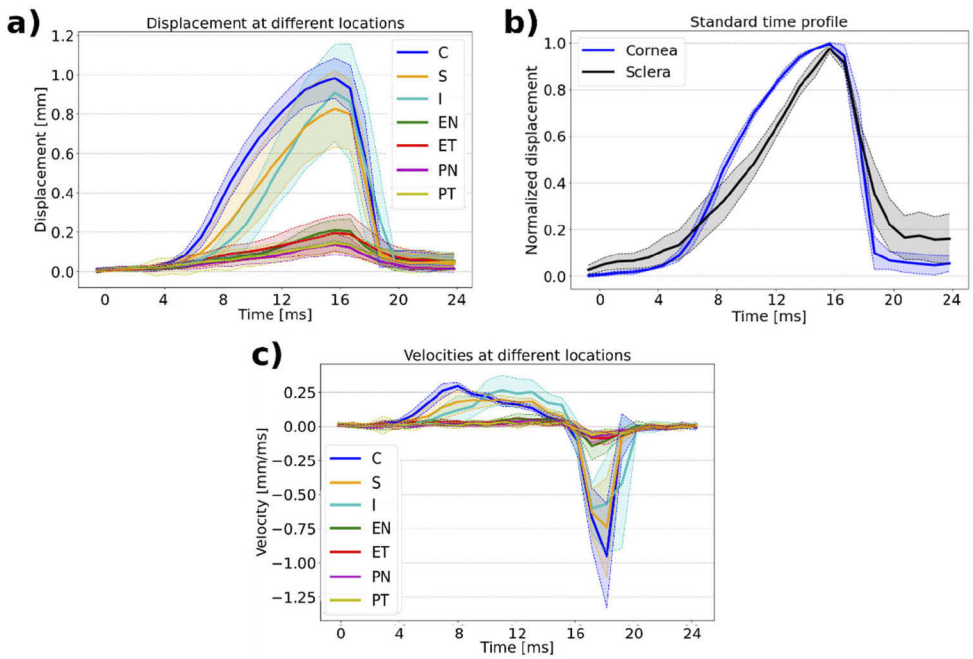

Fig. 5. Average displacement and velocity of the apex vs time at all measured locations during the air-puff deformation event. Both graphs a) and c) come from the same set of measurements and represent at all measured locations a) the displacement vs. time in mm, and c) the velocity vs time, in mm/ms. Figure 5 b) shows the STP $F_S(t)$ of the sclera (gray) compared to the one of the cornea $F_C(t)$ (dark blue). As in the previous figures, C: Cornea, S: Superior sclera, I: Inferior sclera, EN: Equatorial Nasal sclera, ET: Equatorial Temporal sclera, PN: Posterior Nasal sclera, PT: Posterior Temporal sclera.

3. Results

3.1. Maximum apex deformation at different ocular locations

When investigating the apex deformation at all ocular locations, a test-retest reliability analysis indicated a high degree of agreement of the three repeated measurements for each eye and each location (calculated Cronbach´s alpha between 0.968 and 0.996). Figure 4 shows the amplitude of maximum deformation, averaged across the five eyes, to air-puff excitation in the cornea and in the sclera, revealing large differences across locations, ranging from 0.14 ± 0.05 mm (PN) to 0.98 ± 0.10 mm (C). The largest mean value for the deformation was measured at the cornea

Biomedical Optics EXPRESS

(0.98 ± 0.10 mm), followed by the inferior and superior sclera, with a deformation of 0.92 ± 0.26 mm and 0.83 ± 0.19 mm respectively. The deformation was lower for the equatorial nasal and equatorial temporal locations (EN 0.21 ± 0.06 mm and ET 0.20 ± 0.10 mm), and lowest for the posterior part of the eye, with an average maximum deformation of 0.15 ± 0.04 mm on the temporal side (PT) and 0.14 ± 0.05 mm on the nasal side.

From Fig. 4 we can see that the results for maximum deformation appear to be clustered into two groups, namely C, I, and S; and ET, EN, PT, and PN. Statistically significant differences could be seen using Friedmańs test (significance values adjusted by the Bonferroni correction for multiple comparisons) between PN and C, S, and I (adjusted sigma < 0.05).

3.2. Temporal profile of the apex position

We evaluated the dynamic behavior of the deformation through the temporal profile of the apex displacement, which we obtained from the experimental data. Figure 5(a) shows the displacements as a function of time for the different ocular locations, averaged across samples. On average, the deformation peaks at around the same time for all locations, reaching its maximum value at 15.6 ± 0.6 ms. A visual inspection of Fig. 5(b) shows that the shape of the temporal deformation profile of the cornea (dark blue line) differs from that of the sclera, suggesting differences in the biomechanical properties of corneal and scleral tissue. The corneal deformation profile shows a steep incline during the first few ms of deformation. At 11 ms, for example, the sclera has reached half of its maximum displacement (50 ± 6%), while the cornea has already reached 70 ± 8% of it.

Figure 5(c) shows the derivatives of the graphs in Fig. 5(a), which correspond to the velocity of the apex of the cornea and sclera at different locations, as a function of time. The cornea reaches the maximum velocity earlier (at 7.4 ± 0.6 ms) than most scleral locations (at 11.8 ± 1.4 ms, on average). In contrast, both cornea and most scleral locations reach the maximum return velocity at about the same time (17.6 ± 0.6 ms for the cornea, and 17.0 ± 0.6 ms for the sclera). Table 1 gives the maximum apex velocity before and after maximum deformation for all given locations. The absolute velocity is higher when the tissue is returning to the starting position than when it is being deformed by the air-puff pressure, and the maximum deformation velocity is higher for the cornea than for the sclera.

Table 1. Maximum apex velocities v_{max} before and after max. deformation

Location	C	S	I	EN	ET	PN	PT
$\lvert v_{max} \rvert$ before max. def. [m/s]	0.15 ± 0.02	0.10 ± 0.02	0.13 ± 0.06	0.03 ± 0.02	0.02 ± 0.01	0.02 ± 0.01	0.02 ± 0.01
$\lvert v_{max} \rvert$ after max. def. [m/s]	0.48 ± 0.19	0.37 ± 0.18	0.30 ± 0.09	0.07 ± 0.05	0.05 ± 0.02	0.04 ± 0.02	0.04 ± 0.02

Across scleral locations, superior and inferior sclera show around 450-550% higher velocity than equatorial nasal and temporal, and 575-825% more than posterior nasal and temporal (See Table 1).

We further investigated the temporal evolution at all locations within the incoming deformation phase, *i.e.* until t=15 ms, when all deformations are at maximum amplitude. An ANOVA test on all locations between 0 ms and 15 ms showed significant differences of some locations emerging at t=4 ms, which was then defined as the starting point of the investigated ingoing deformation phase. We rescaled the values of all functions in Fig. 5(a) by dividing each function by its maximum. We observed that during the above defined ingoing deformation phase (between t=4 ms and t=15 ms) the normalized scleral temporal deformation functions $f_j(t)$ (at different locations j=1. . . 6) all evolved different with respect to the corneás temporal deformation function.

Biomedical Optics EXPRESS

Indeed, all normalized scleral deformation functions $f_j(t)$, divided by their maximum value, fit the same profile $F_S(t)$ (regression model, reference C, R=0.926, and Durbin-Watson 1.719). We therefore defined $F_S(t)$ for the sclera:

$$F_s(t) := \frac{1}{6}\sum_{j=1}^{6}\frac{f_j(t)}{max(f_j)} \tag{2}$$

and named $F_S(t)$ the sclerás Standard Time Profile (STP). Figure 5(b) shows $F_S(t)$ and the equivalent time profile for the cornea $F_C(t)$. The visually obvious difference between corneal and scleral Standard Time Profile (STP) can then be quantified using the unstandardized coefficients of a quadratic regression model that describes the shape of the ingoing deformation phase. In summary, within the model, R was 0.991 for the cornea (Durbin-Watson 0.995), and 0.926 for all scleral locations (Durbin-Watson 1.719). The most relevant finding is that the corneal profile $F_C(t)$ has a positive coefficient for the linear, and a negative coefficient for the quadratic part of the regression model, while the opposite was found for $F_S(t)$. In other words, while the shape of the ingoing deformation phase of the corneal STP is convex, it is concave for the sclera. In Fig. 5(b) we can visually observe this. When quantifying all scleral functions $f_j(t)$ individually (not shown), we can observe that all scleral functions remain close to its STP $F_S(t)$, with location I being the most different one (with a quadratic coefficient of 0.06 ± 0.02 compared to the 0.03 ± 0.01 for $F_S(t)$). On the other hand, the corneal time profile differs more, with a quadratic coefficient of -0.04 ± 0.01.

3.3. Arc length during the deformation event

The study of the evolution and change in arc length (as defined in section 2.5) allowed us to investigate compression and extension rates during the air-puff deformation event. Figure 6 compares the difference in arc length between the tissue's resting position and its length at deformation at all-time points during the deformation event for all seven locations. The black vertical line at 15.6 ms indicates approximately the time at maximum deformation.

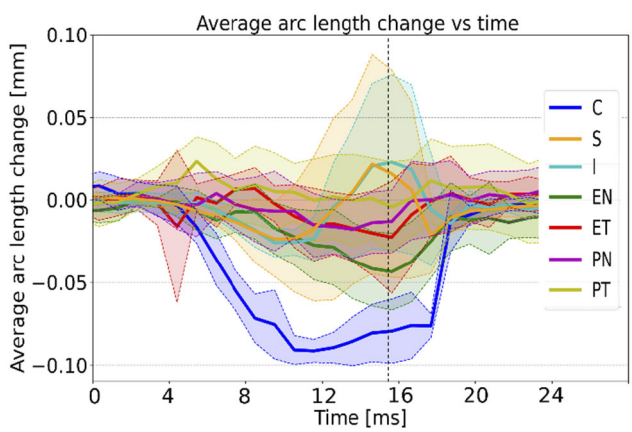

Fig. 6. Arc length change versus time during the deformation event. The labels follow the code of Fig. 1(a).

Figure 6 shows that there is an initial compression (decrease in arc length) between the 0-10 ms at all locations except for the posterior temporal sclera. From the data it is apparent that, in the superior and inferior part of the sclera, this compression is followed by an extension of the material that continues until the time of maximum deformation. Interestingly, these two locations are the only ones that present an extension at maximum deformation compared to the initial arc

Biomedical Optics EXPRESS

length. In the cornea, there is also a slight extension after the initial compression, but contrary to the superior and inferior sclera, this extension does not reach the arc length at initial resting position. In all other locations (EN, ET, PN, and PT) the deformation event consists of an overall compression. After reaching maximum deformation, the arc length returns, in all cases, to its initial value as the deformation finishes.

Superior and inferior sclera, which had shown the highest apex displacements among the scleral locations, also present an increase in the arc length at maximum deformation (around 0.5% extension). Equatorial and posterior regions, which had shown lower apex displacements, present a decrease in arc length (between 0.7% and 0.1% compression). The cornea is the location that shows the largest change in the arc length (1.6% compression). Even though the cornea also presents an overall compression during the deformation event, its maximum compression (1.6%) does not occur at maximum deformation (1.4% compression).

3.4. FEM simulations

FEM inverse optimizations were applied as described in Section 2.4 to retrieve the material properties of the tissue at the six different locations studied. A summary of the reconstructed parameters is shown in Table 2.

Table 2. Biomechanical parameters obtained from FEM inverse optimization.

	Young's Modulus [MPa]	C_{10} [MPa]	C_{20} [MPa]
Sclera			
Inferior	1.838	0.257	2.070
Superior	2.194	0.269	3.773
Equatorial Temporal	6.037	0.992	4.379
Equatorial Nasal	4.402	0.833	1.386
Posterior Temporal	4.535	0.749	0.228
Posterior Nasal	4.896	1.255	0.181
Cornea	0.687	0.055	2.141

The secant Young's modulus was estimated from the simulated stress-strain curve (calculated using the reconstructed coefficients for the Yeoh material model at uniaxial extension), with strain at 9%. Figure 7 shows the estimated Youngś Moduli (YM) at the cornea and different scleral locations. The YM of the cornea is 0.69 ± 0.14 MPa while the lowest scleral YM are found for the inferior and superior sclera (1.84 ± 0.30 MPa and 2.19 ± 0.43 MPa), the sclera being at least 2.7 times stiffer than the cornea. The estimated Young's Moduli of the other scleral locations (EN, ET, PN, PT) is above 4 MPa and doubles the one estimated for the superior and inferior scleral locations, the maximum stiffness is found for the equatorial temporal sclera, with a YM of 6.04 ± 2.11 MPa. On average, the scleral stiffness is 5.8 times the corneal one. Confidence intervals (CI) were calculated and compared for the five samples. As before, the cornea showed the most homogeneous behavior with the smallest confidence intervals. It should be noted that, while in the experimental data we could separate the data into two clusters, here, the cornea separates itself even more from I and S, and ET, EN, PT, PN.

The estimated C_{10} (overall stiffness) ranged from 0.055 MPa for the cornea to 1.249 MPa for the posterior nasal position. The C_{20} (related to the non-linear stress-strain response) ranged from 0.185 MPa for the scleral posterior temporal location to 4.379 MPa for the equatorial temporal location. The ratio C_{20}/C_{10} was higher for the cornea (39) than for the scleral positions (0.14-14), indicating a larger non-linear response.

Biomedical Optics EXPRESS

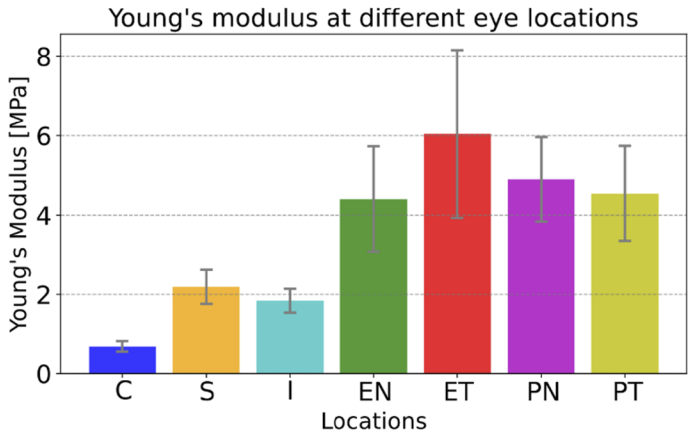

Fig. 7. Average Young modulus at 10% strain at all locations. The colors correspond to the colors used within the sketch of the eye in Fig. 4.

4. Discussion

In this study, we have used a novel SSOCT imaging system, coupled with air-puff excitation [53] to investigate scleral deformation behavior at different locations of the ocular globe. The corneal deformation behavior, which has been investigated previously (see section 4.1), was used to draw comparisons with the sclera and conclude about overall ocular deformation behavior. To the best of our knowledge, this is the first time that the use of APDI has been reported in the sclera. Our findings suggest that in scleral tissue, the maximum deformation amplitude and the deformation profile in time differs substantially from that of the cornea. Also, while we found differences across scleral locations in various parameters, including maximum deformation and arc length, other parameters such as time to maximum deformation or velocity were very similar across locations. When comparing corneal and scleral deformation behavior in time, we could identify a sclera time profile that was similar across all scleral locations, but differed significantly from that of the cornea. The differences in material properties across the different scleral locations and cornea were also reflected in the material parameters reconstructed by FEM inverse optimization, indicating that the differences in the maximum deformation do not arise only from differences in tissue thickness, but also from inherent mechanical properties of the tissue.

Our customized air-puff SSOCT instrument was well suited to investigate scleral deformation. The system's spatial transverse sampling resolution was set at 234 µm as covering a large transverse field of view was deemed more important than finer sampling, as spatial deformation profile features are unlikely to change over a finer scale. In the future, the large transverse field of view of 15 mm will allow a more complete analysis of the deformation event than earlier presented OCT devices [49–52], and commercially available air-puff deformation imaging devices which typically have a horizontal coverage of 8.5mm [48]. However, in case a higher spatial transverse sampling resolution is required, one could increase the laser sweep rate, without compromising the temporal resolution. The system's temporal sampling of ocular deformation of 1 ms was found to be enough to differentiate the deformation profiles for both sclera and cornea within a deformation event lasting several milliseconds. Nevertheless, in case a higher temporal resolution is required, one could reduce the transverse field of view to a smaller ocular region. The ultra-fast transverse scanning pattern repetition frequency of 1 kHz of our instrument would also make it possible to image the deformation events over an enlarged field of view, not only horizontally, but also vertically. This will open up possibilities to investigate scleral deformation in multiple meridians, and given reported differences in collagen arrangement or regional variations in

Biomedical Optics EXPRESS

the orientation of collagen bundles [11], a different deformation behavior may be found across different meridians.

4.1. Deformation magnitudes

In previous studies, APDI has been successfully applied to study the biomechanics of the cornea *ex-vivo* [52,54] and *in-vivo* [48,49,52,54,71] either with the commercial Scheimpflug-based Corvist ST [48,54,71], or laboratory-based OCT systems [49,52]. For *ex vivo* porcine corneas, a maximum corneal apex displacement of 1.221 ± 0.43 mm at IOP=15 mmHg [54], and 0.85 ± 0.26 mm at IOP=18mmHg [52] was reported for an air-puff of similar pressure. Our results indicate a maximum corneal apex displacement of 0.98 ± 0.10 mm, matching the previous results of the literature.

Scleral maximum deformation varied drastically across scleral locations, being around 6 times lower in the posterior sclera than in the superior and inferior sclera. Besides inherent differences in the tissue mechanical properties (described below), and for a constant IOP, it is likely that these differences also reflect spatial variations in the tissue thickness, which are particularly relevant in porcine eyes. While the corneal thickness is almost constant (0.96 mm, on average [65]), the thickness of the porcine sclera varies significantly, with the thickest parts of the sclera found near the limbus (0.91 mm) [65,68], at the posterior part, and in the optical nerve region (0.78 ± 0.09 mm and 1.00 ± 0.09 mm respectively) [65]. The thinnest part is approximately 5 mm from the limbus (between 0.35 ± 0.10 mm [68] and 0.58 ± 0.13 mm [65]). The reported higher thickness of the posterior part of the porcine sclera explains, in part, the observed low deformation amplitude. On a note for future applications in human tissue, regional variations (nasal, temporal, inferior and superior) in scleral thickness in human eye globes have been suggested, but not conclusively identified [72]. Apart from the thickness profile, the porcine eye globe is elliptically shaped. While the nasal-temporal and superior-inferior globe diameters are similar (around 25.48 mm and 24.48 mm, respectively), the axial diameter is up to about 15% shorter (about 21.64 mm) [73], hence, the radius of curvature at the globe equator is larger than the radius of curvature at the posterior eye globe, this geometrical differences could affect the response to the air-puff.

Other potential underlying causes for the regional variations in scleral max. deformation amplitude may include localized differences in collagen arrangement or regional variations in the orientation of collagen bundles, as found, for example in the human sclera [74–76].

We have also investigated and compared the corneal and scleral (apex) deformation profiles in time during air-puff excitation. It is encouraging to compare our results for the cornea with the ones obtained in human eyes [48,77,78] and porcine eyes [48,49]. The extent of the deformation event (around 17 ms) is similar to the one found by Dorronsoro et al. [52] (17.3 ± 1.2 ms), and the general behavior in deformation velocity, i.e., an increase and decrease in deformation velocity before and after maximum deformation, with the maximum velocity occurring at regression to resting position, has been found in numerous human studies [78].

In all scleral locations, the apex deformation in time shows a common profile that differs from the corneal one, this difference is most pronounced when normalizing the deformation functions by their maximum. The resulting time profile, which we refer to as the scleral Standard Time Profile (STP), seems to be independent of regional variations in scleral thickness. While we have investigated only one configuration of the air-puff acting on untreated eyes, further research is needed to study how this profile depends on the air-puff parameters (strength and duration of the pulse) and how it is affected by the biomechanical properties of the tissue.

The arc length change with time, which is related to possible compression and extension behavior during air puff excitation, presents differences between both the cornea and sclera, and between the different scleral locations. The arc length has recently been investigated and implemented in the current software of the before-mentioned OCULUS Corvis ST [79], which reports a delta value that describes the change of the arc length between the initial state and

Biomedical Optics EXPRESS

the highest concavity moment during the air-puff excitation event, in a defined 7 mm zone [78,80]. Here, the arc length is defined over a 5.6 mm zone. In line with the results of maximum deformation, there are important differences in arc length when comparing superior and inferior location with the equatorial and posterior locations. While the equatorial (nasal and temporal) and posterior (nasal) scleral tissue seems to go through a compression during deformation, the superior/inferior locations reaches a state with an overall extension. The posterior temporal sclera shows an almost constant arc length through the measurement. A possible explanation for this behavior might be related to the microarchitecture of the sclera from which the macroscale deformation behavior arises. The sclera is composed of collagen fibrils of various diameters that are interwoven and form bundles that vary in width and thickness [11]. The orientation of the fibrils is highly dependent on the region, the IOP, and the pull of the extraocular muscles [81]. The collagen bundles are lamellar in nature and are interwoven, and the interweaving is again dependent on the position in the sclera [82]. Recently, numerical models could show that collagen fiber interweaving is central to sclera stiffness [83], implicating that biomechanical behavior might be dependent on the degree of the interweaving collagen *lamellae*, which in turn could affect deformation behavior.

4.2. Biomechanical properties

We have obtained biomechanical properties of the ocular tissue using inverse optimization techniques based on a FE model. Biomechanical properties like the Young's Modulus (YM), together with differences in the eye's geometry and tissue thickness are contributing factors to differences in the air-puff tissue deformation patterns [54]. Our obtained values for the YM is in general agreement with reported values in the literature [84], in particular with the well accepted higher stiffness of the sclera when compared to the cornea. Prior studies have shown a wide range of values for the YM of the porcine cornea, e.g., 0.8-2.6 MPa using extensiometry [63], 0.24-3.90 MPa using eye inflation [85], and 0.99-1.59 MPa using air-puff experiments [60]. For the sclera, studies using extensiometry estimated a YM between 1.95 ± 1.84 MPa for a 4% strain [84] and 5.2 ± 3.0 MPa for low strains [77]. These studies have noted that the YM increases with the percentage of strain, suggesting non-linear properties. Our YM values are in the lower range of previous reports, which coincides with the relatively small change in the arc length, as shown in Section 3.3 (between a maximum 1.6% compression and 0.5% extension), situating our experiment in a low strain regime.

We found that the temporal-nasal locations are stiffer (5.22 ± 0.82 MPa) than the superior-inferior (2.02 ± 0.18 MPa). The posterior positions (at 20° angle from equator) had lower moduli on average (4.72 ± 0.18 MPa) than the temporal and nasal positions, in good agreement with the trend observed in previous stress-strain studies [86], although the previous study reports modulus for the equatorial nasal position lower than the posterior moduli.

There are many material models in the literature for the eye tissue [57]. Linear viscoelastic [59] or hyperelastic Mooney-Rivlin [60] material models have previously been used to reconstruct the biomechanical properties of the cornea after an air-puff induced deformation. More complex material models can be used to account for the complex microstructure of the collagen fibers that make up the tissue, as it was done by other authors in posterior human sclera [87]. In the current study, similarly to [88], we have used a Yeoh material model for a description of the material properties of cornea and sclera (simplified to 2 parameters instead of 3). This added complexity in the material model captures the larger non-linearity of the corneal material's behavior, accounting for the difference in the shape of the deformation. In future models, the finding of the scleral STP could be used to fix the non-linear behavior in the material model and solve the optimization with a material model with less material constants.

A limitation in modeling is the effect of the tissue's thickness on the response. The model used to retrieve material parameters was rotationally symmetric. Differences in the thickness

Biomedical Optics EXPRESS

profile of temporal/nasal and inferior/superior positions in the sclera might lead to understating or overstating differences in material properties. Nonetheless, the retrieved parameters can be used to assess overall stiffness.

4.3. Implications, limitations, and future work

The reconstruction of the mechanical properties of both cornea and sclera from SSOCT-based air-puff imaging represents a leap forward in the non-invasive biomechanical assessment of ocular tissue, since the evaluation on intact eyes prevents the loss of the ocular mechanical integrity. Air-puff stimulation is a conventional practice in corneal clinical evaluation, and it is conceivably applicable *in vivo* in the sclera by means of eccentric fixation or eye rotation, at least in regions around the limbus. A practical limitation of this technique *in vivo* is the difficult access to the posterior region, the area most subject to elongation in myopia development. Despite this constraint, the similarities observed between all the scleral locations in the STP might indicate that changes in biomechanical properties of the posterior sclera could be reflected and measured in the anterior sclera, which is more easily accessible.

The current study did not attempt to map scleral properties in a large sample of porcine eyes, but rather present an effective alternative to measure deformation parameters and inherent mechanical properties of the cornea and sclera, in the same globe. Further studies are needed to confirm the use of the presented technology, both in animal models and human globes, and potentially establish the relationship between mechanical properties of anterior and posterior regions, as a function of refractive error and age.

In the future, the presented technology could be used to assess the potential effects on scleral biomechanics during myopia development, for example with myopia that is induced through lens-wearing or form-deprivation. In addition, the effects of scleral cross-linking (SXL) can be evaluated in similar ways using air-puff deformation imaging as those used to assess the efficiency of corneal cross-linking (CXL).

In this context, it is interesting to point to the current advances in wave-based OCE imaging, as it has been presented in the cornea [38,89,90] and, more recently, in the sclera *ex vivo* [40] and *in vivo* [41]. Wave-based OCE excites shear waves, which are tracked using phase-sensitive OCT. The tissués shear modulus can then be calculated with the shear wave group velocity. The additional information of the sclerás shear modulus, and its relation to the Youngś modulus is beyond the scope of this paper but are of high interest in future investigations on ocular biomechanics.

In addition, we have evaluated specific deformation parameters, some of which have been studied previously in the cornea, including their association to mechanical properties, corneal thickness, or IOP. We did not attempt to evaluate all multiple parameters extracted from temporal and spatial deformation images. Future research is needed to further investigate the defined STPs for both sclera and cornea, specifically their dependence on variation in IOP and tissue biomechanics. Both properties can be controlled easily *ex vivo* (via an IOP control system and localized alteration of biomechanical properties with SXL/CXL or collagenase application [91]).

Another evaluated parameter in this study was the arc length that was defined in a predetermined scanning window. The measurement of the arc length is well suited for the cornea since the limbus acts as a semi-fixed boundary between cornea and sclera. In fact, the enlarged scanning field of view of our SSOCT system would allow the analysis of the arc length within these boundaries, which should be considered for future research. On the other hand, in the sclera there are not these natural boundaries and our reference points at 2.8 mm from the apex do not constitute fixed boundaries. Even though no deformation outside these points was observed, the fact that the arc length is analyzed on a quasi-boundary-free surface imposes that these results must be interpreted with caution.

Biomedical Optics EXPRESS

In summary, this study presents for the first time corneal and scleral mechanical properties from air-puff deformation imaging, obtained in the same eye globe, *ex vivo*. The presented FEM simulations and material property reconstructions give insights on the most suitable mechanical model to represent each tissue, and intrinsic differences between parameters. Although in our modeling cornea and sclera were treated independently, it has been recognized that the observed air-puff corneal deformation pattern depends in part on the mechanical properties of the sclera [62], and likely in reverse. A joint cornea/sclera reconstruction, incorporating the deformation patterns of both cornea and sclera is also conceivable. Advances in this direction are applicable in the management of glaucoma.

The importance of the study lies in the demonstration of a non-invasive technique that allows to measure biomechanical properties of the sclera (and cornea). This technique has prospective impactful implications, as it could serve as a first step towards *in vivo* measurements, becoming a tool to monitor myopia progression, track the efficiency of emerging myopia treatments and management of glaucoma.

Funding. European Research Council (2018-ADG-SILKEYE-833106); Horizon 2020 Framework Programme European Project Multiply (H-2020-MSCACOFUND-2015 Ref. 713694); Spanish Government (FIS2017-84753-R); Horizon 2020 Framework Programme European Project Imcustomeye (H2020-ICT-2017 Ref. 779960); Spanish Government (CSIC JAE Intro Fellowship); L'Oréal-UNESCO "For Women in Science" Spain; Spanish Government Juan de la Cierva-Incorporation Fellowship (IJC2018-037508-I); Fundacja na rzecz Nauki Polskiej (MAB/2019/12); National Agency for Academic Exchange, Polish Government (NAWA ULAM/2020/1/00176).

Acknowledgments. The authors would like to thank Dr. Ashkan Eliasy (School of Engineering, The University of Liverpool, UK) for fruitful discussions on FEM modelling and scleral biomechanics, Dr. Alberto de Castro (IO-CSIC, Spain) for thorough discussions on minimization algorithms, and Dr. Laura Barrios (Computing Center, SGAI-CSIC, Spain) and Prof. Matteo Bonforte (Department of Mathematics UAM and ICMAT, Spain) for the support in the statistical analysis of our data and crucial discussions on the interpretation of the STPs.

Disclosures. Patent disclosures: FN00649590 (JSB, AC, SM); WO2012146811A1 (SM)

Data availability. Data underlying the results presented in this paper are not publicly available at this time but may be obtained from the authors upon reasonable request.

References

1. N. A. McBrien and A. Gentle, "Role of the sclera in the development and pathological complications of myopia," Prog. Retin. Eye Res. **22**(3), 307–338 (2003).
2. B. A. Holden, T. R. Fricke, D. A. Wilson, M. Jong, K. S. Naidoo, P. Sankaridurg, T. Y. Wong, T. J. Naduvilath, and S. Resnikoff, "Global prevalence of myopia and high myopia and temporal trends from 2000 through 2050," Ophthalmology **123**(5), 1036–1042 (2016).
3. E. Dolgin, "The myopia boom," Nature **519**(7543), 276–278 (2015).
4. K. Zadnik, "Myopia development in childhood," Optom. Vis. Sci. **74**(8), 603–608 (1997).
5. G. Muralidharan, E. Martínez-Enríquez, J. Birkenfeld, M. Velasco-Ocana, P. Pérez-Merino, and S. Marcos, "Morphological changes of human crystalline lens in myopia," Biomed. Opt. Express **10**(12), 6084–6095 (2019).
6. D. O. Mutti, G. L. Mitchell, L. T. Sinnott, L. A. Jones-Jordan, M. L. Moeschberger, S. A. Cotter, R. N. Kleinstein, R. E. Manny, J. D. Twelker, and K. Zadnik, "Corneal and crystalline lens dimensions before and after myopia onset," Optom. Vis. Sci. **89**(3), 251–262 (2012).
7. L. F. Garner, M. Yap, and R. Scott, "Crystalline lens power in myopia," Optometry and Vision Science **69**(11), 863–865 (1992).
8. A. Consejo and J. J. Rozema, "In vivo anterior scleral morphometry, axial length and myopia," Contact Lens Anterior Eye **43**(1), 21–25 (2020).
9. H. Niyazmand, S. A. Read, D. A. Atchison, and M. J. Collins, "Anterior eye shape in emmetropes, low to moderate myopes, and high myopes," Contact Lens Anterior Eye (2020).
10. J. T. Siegwart Jr and T. T. Norton, "Regulation of the mechanical properties of tree shrew sclera by the visual environment," Vision Res. **39**(2), 387–407 (1999).
11. Y. Komai and T. Ushiki, "The three-dimensional organization of collagen fibrils in the human cornea and sclera," Invest. Ophthalmol. Vis. Sci. **32**, 2244–2258 (1991).
12. A. J. Bailey, "Structure, function and ageing of the collagens of the eye," Eye **1**(2), 175–183 (1987).
13. B. J. Curtin and C. C. Teng, "Scleral changes in pathological myopia," Trans. Acad. Ophthalmol. Otolaryngol. Am. Acad. Ophthalmol. Otolaryngol. **62**, 777–788 (1958).
14. B. J. Curtin, T. Iwamoto, and D. P. Renaldo, "Normal and staphylomatous sclera of high myopia: an electron microscopic study," Arch. Ophthalmol. **97**(5), 912–915 (1979).

Biomedical Optics EXPRESS

15. A. Gentle, Y. Liu, J. E. Martin, G. L. Conti, and N. A. McBrien, "Collagen gene expression and the altered accumulation of scleral collagen during the development of high myopia," J. Biol. Chem. **278**(19), 16587–16594 (2003).
16. J. R. Phillips, M. Khalaj, and N. A. McBrien, "Induced myopia associated with increased scleral creep in chick and tree shrew eyes," Invest. Ophthalmol. Vis. Sci. **41**, 2028–2034 (2000).
17. G. Wollensak, E. Spoerl, and T. Seiler, "Riboflavin/ultraviolet-A–induced collagen crosslinking for the treatment of keratoconus," Am. J. Ophthalmol. **135**(5), 620–627 (2003).
18. D. Cherfan, E. E. Verter, S. Melki, T. E. Gisel, F. J. Doyle, G. Scarcelli, S. H. Yun, R. W. Redmond, and I. E. Kochevar, "Collagen cross-linking using rose bengal and green light to increase corneal stiffness," Invest. Ophthalmol. Vis. Sci. **54**(5), 3426–3433 (2013).
19. N. Bekesi, I. E. Kochevar, and S. Marcos, "Corneal biomechanical response following collagen cross-linking with Rose Bengal–green light and Riboflavin-UVA," Invest. Ophthalmol. Vis. Sci. **57**(3), 992–1001 (2016).
20. N. Bekesi, P. Gallego-Munoz, L. Ibares-Frias, P. Perez-Merino, M. C. Martinez-Garcia, I. E. Kochevar, and S. Marcos, "Biomechanical changes after in vivo collagen cross-linking with rose bengal–green light and riboflavin-UVA," Invest. Ophthalmol. Vis. Sci. **58**(3), 1612–1620 (2017).
21. J. A. Germann, E. Martínez-Enríquez, M. C. Martínez-García, I. E. Kochevar, and S. Marcos, "Corneal collagen ordering after in vivo rose bengal and riboflavin cross-linking," Invest. Ophthalmol. Vis. Sci. **61**(3), 28 (2020).
22. J. A. Germann, E. Martinez-Enriquez, and S. Marcos, "Quantization of collagen organization in the stroma with a new order coefficient," Biomed. Opt. Express **9**(1), 173–189 (2018).
23. C. Schuldt, A. Karl, N. Körber, C. Koch, Q. Liu, A. W. Fritsch, A. Reichenbach, P. Wiedemann, J. A. Käs, and M. Francke, and others, "Dose-dependent collagen cross-linking of rabbit scleral tissue by blue light and riboflavin treatment probed by dynamic shear rheology," Acta Ophthalmol. **93**(5), e328–e336 (2015).
24. A. Dotan, I. Kremer, T. Livnat, A. Zigler, D. Weinberger, and D. Bourla, "Scleral cross-linking using riboflavin and ultraviolet-a radiation for prevention of progressive myopia in a rabbit model," Exp. Eye Res. **127**, 190–195 (2014).
25. H. P. Iseli, N. Körber, A. Karl, C. Koch, C. Schuldt, A. Penk, Q. Liu, D. Huster, J. Käs, and A. Reichenbach, and others, "Damage threshold in adult rabbit eyes after scleral cross-linking by riboflavin/blue light application," Exp. Eye Res. **139**, 37–47 (2015).
26. M. Wang, F. Zhang, K. Liu, and X. Zhao, "Safety evaluation of rabbit eyes on scleral collagen cross-linking by riboflavin and ultraviolet A," Clin Experiment Ophthalmol **43**(2), 156–163 (2015).
27. S. Liu, S. Li, B. Wang, X. Lin, Y. Wu, H. Liu, X. Qu, J. Dai, X. Zhou, and H. Zhou, "Scleral cross-linking using riboflavin UVA irradiation for the prevention of myopia progression in a guinea pig model: blocked axial extension and altered scleral microstructure," PLoS One **11**, e0165792 (2016).
28. A. T. Broman, N. G. Congdon, K. Bandeen-Roche, and H. A. Quigley, "Influence of corneal structure, corneal responsiveness, and other ocular parameters on tonometric measurement of intraocular pressure," J. Glaucoma **16**(7), 581–588 (2007).
29. J. Liu and C. J. Roberts, "Influence of corneal biomechanical properties on intraocular pressure measurement: quantitative analysis," J. Cataract Refract. Surg. **31**(1), 146–155 (2005).
30. D. R. Lari, D. S. Schultz, A. S. Wang, O. T. Lee, and J. M. Stewart, "Scleral mechanics: Comparing whole globe inflation and uniaxial testing," Exp. Eye Res. **94**(1), 128–135 (2012).
31. A. Elsheikh and K. Anderson, "Comparative study of corneal strip extensometry and inflation tests," J. R. Soc. Interface. **2**(3), 177–185 (2005).
32. A. Elsheikh, B. Geraghty, D. Alhasso, J. Knappett, M. Campanelli, and P. Rama, "Regional variation in the biomechanical properties of the human sclera," Exp. Eye Res. **90**(5), 624–633 (2010).
33. S. Backhouse and A. Gentle, "Scleral remodelling in myopia and its manipulation: a review of recent advances in scleral strengthening and myopia control," Ann. Eye Sci **3**, 5 (2018).
34. K. M. Myers, B. Coudrillier, B. L. Boyce, and T. D. Nguyen, "The inflation response of the posterior bovine sclera," Acta Biomater. **6**(11), 4327–4335 (2010).
35. C. Whitford, A. Joda, S. Jones, F. Bao, P. Rama, and A. Elsheikh, "Ex vivo testing of intact eye globes under inflation conditions to determine regional variation of mechanical stiffness," Eye and Vis **3**(1), 21 (2016).
36. M. A. Kirby, I. Pelivanov, S. Song, L. Ambrozinski, S. J. Yoon, L. Gao, D. Li, T. T. Shen, R. K. Wang, and M. O'Donnell, "Optical coherence elastography in ophthalmology," J. Biomed. Opt. **22**(12), 1 (2017).
37. K. V Larin and D. D. Sampson, "Optical coherence elastography–OCT at work in tissue biomechanics," Biomed. Opt. Express **8**(2), 1172–1202 (2017).
38. Z. Jin, S. Chen, Y. Dai, C. Bao, S. Ye, Y. Zhou, Y. Wang, S. Huang, Y. Wang, and M. Shen, "In vivo noninvasive measurement of spatially resolved corneal elasticity in human eyes using Lamb wave optical coherence elastography," J. Biophotonics **13**, e202000104 (2020).
39. G. Scarcelli, R. Pineda, and S. H. Yun, "Brillouin optical microscopy for corneal biomechanics," Invest. Ophthalmol. Vis. Sci. **53**(1), 185–190 (2012).
40. F. Zvietcovich, A. Nair, M. Singh, S. R. Aglyamov, M. D. Twa, and K. V Larin, "Dynamic optical coherence elastography of the anterior eye: understanding the biomechanics of the limbus," Invest. Ophthalmol. Vis. Sci. **61**(13), 7 (2020).
41. A. Ramier, A. M. Eltony, Y. Chen, F. Clouser, J. S. Birkenfeld, A. Watts, and S.-H. Yun, "In vivo measurement of shear modulus of the human cornea using optical coherence elastography," Sci. Rep. **10**(1), 17366–10 (2020).

Biomedical Optics EXPRESS

42. P. Shao, A. M. Eltony, T. G. Seiler, B. Tavakol, R. Pineda, T. Koller, T. Seiler, and S.-H. Yun, "Spatially-resolved Brillouin spectroscopy reveals biomechanical abnormalities in mild to advanced keratoconus in vivo," Sci. Rep. **9**, 1–12 (2019).
43. P. Shao, S. Besner, J. Zhang, G. Scarcelli, and S.-H. Yun, "Etalon filters for Brillouin microscopy of highly scattering tissues," Opt. Express **24**(19), 22232–22238 (2016).
44. C. J. Roberts, A. M. Mahmoud, J. P. Bons, A. Hossain, A. Elsheikh, R. Vinciguerra, P. Vinciguerra, and R. Ambrósio Jr, "Introduction of two novel stiffness parameters and interpretation of air Puff–Induced biomechanical deformation parameters with a dynamic scheimpflug analyzer," J. Refract. Surg. **33**(4), 266–273 (2017).
45. A. Eliasy, K.-J. Chen, R. Vinciguerra, O. Maklad, P. Vinciguerra, R. Ambrósio Jr, C. J. Roberts, and A. Elsheikh, "Ex-vivo experimental validation of biomechanically-corrected intraocular pressure measurements on human eyes using the CorVis ST," Exp. Eye Res. **175**, 98–102 (2018).
46. R. Vinciguerra, R. Ambrósio Jr, A. Elsheikh, C. J. Roberts, B. Lopes, E. Morenghi, C. Azzolini, and P. Vinciguerra, "Detection of keratoconus with a new biomechanical index," J. Refract. Surg. **32**(12), 803–810 (2016).
47. J. J. Pitre, M. A. Kirby, D. S. Li, T. T. Shen, R. K. Wang, M. O'Donnell, and I. Pelivanov, "Nearly-incompressible transverse isotropy (NITI) of cornea elasticity: model and experiments with acoustic micro-tapping OCE," Sci. Rep. **10**(1), 12983–14 (2020).
48. J. Hong, J. Xu, A. Wei, S. X. Deng, X. Cui, X. Yu, and X. Sun, "A new tonometer—the Corvis ST tonometer: clinical comparison with noncontact and Goldmann applanation tonometers," Invest. Ophthalmol. Vis. Sci. **54**(1), 659–665 (2013).
49. D. Alonso-Caneiro, K. Karnowski, B. J. Kaluzny, A. Kowalczyk, and M. Wojtkowski, "Assessment of corneal dynamics with high-speed swept source optical coherence tomography combined with an air puff system," Opt. Express **19**(15), 14188–14199 (2011).
50. E. Maczynska, J. Rzeszewska-Zamiara, A. J. Villar, M. Wojtkowski, B. J. Kaluzny, and I. Grulkowski, "Air-puff-Induced dynamics of ocular components measured with optical biometry," Invest. Ophthalmol. Vis. Sci. **60**(6), 1979–1986 (2019).
51. A. Jiménez-Villar, E. Mączyńska, A. Cichański, M. Wojtkowski, B. J. Kałużny, and I. Grulkowski, "High-speed OCT-based ocular biometer combined with an air-puff system for determination of induced retraction-free eye dynamics," Biomed. Opt. Express **10**(7), 3663–3680 (2019).
52. C. Dorronsoro, D. Pascual, P. Pérez-Merino, S. Kling, and S. Marcos, "Dynamic OCT measurement of corneal deformation by an air puff in normal and cross-linked corneas," Biomed. Opt. Express **3**(3), 473–487 (2012).
53. A. Curatolo, J. S. Birkenfeld, E. Martinez-Enriquez, J. A. Germann, G. Muralidharan, J. Palací, D. Pascual, A. Eliasy, A. Abass, and J. Solarski, "Multi-meridian corneal imaging of air-puff induced deformation for improved detection of biomechanical abnormalities," Biomed. Opt. Express **11**(11), 6337–6355 (2020).
54. S. Kling and S. Marcos, "Contributing factors to corneal deformation in air puff measurements," Invest. Ophthalmol. Vis. Sci. **54**(7), 5078–5085 (2013).
55. M. L. Salvetat, M. Zeppieri, C. Tosoni, M. Felletti, L. Grasso, and P. Brusini, "Corneal deformation parameters provided by the Corvis-ST Pachy-Tonometer in healthy subjects and glaucoma patients," J. Glaucoma **24**(8), 568–574 (2015).
56. R. Koprowski, "Automatic method of analysis and measurement of additional parameters of corneal deformation in the Corvis tonometer," BioMed Eng OnLine **13**(1), 150 (2014).
57. T. M. Nejad, C. Foster, and D. Gongal, "Finite element modelling of cornea mechanics: a review," Arq. Bras. Oftalmol. **77**(1), 60–65 (2014).
58. A. Elsheikh and D. Wang, "Numerical modelling of corneal biomechanical behaviour," Comput. Methods Biomech. Biomed. Engin. **10**(2), 85–95 (2007).
59. S. Kling, N. Bekesi, C. Dorronsoro, D. Pascual, and S. Marcos, "Corneal viscoelastic properties from finite-element analysis of in vivo air-puff deformation," PLoS One **9**, e104904 (2014).
60. N. Bekesi, C. Dorronsoro, A. de la Hoz, and S. Marcos, "Material properties from air puff corneal deformation by numerical simulations on model corneas," PLoS One **11**(10), e0165669 (2016).
61. J. S. Birkenfeld, A. Curatolo, A. Eliasy, E. Martinez-Enriquez, A. Varea, A. Gonzalez-Ramos, A. Abass, B. T. Lopes, J. Merayo-Lloves, and A. Elsheikh, "Improved detection of corneal deformation asymmetries in keratoconus patients using multi-meridian deformation imaging," Invest. Ophthalmol. Vis. Sci. **62**, 2031 (2021).
62. B. A. Nguyen, C. J. Roberts, and M. A. Reilly, "Biomechanical impact of the sclera on corneal deformation response to an air-puff: a finite-element study," Front. Bioeng. Biotechnol. **6**, 210 (2019).
63. G. Wollensak, E. Spoerl, and T. Seiler, "Stress-strain measurements of human and porcine corneas after riboflavin–ultraviolet-A-induced cross-linking," J. Cataract Refract. Surg. **29**(9), 1780–1785 (2003).
64. G. Wollensak and E. Spoerl, "Collagen crosslinking of human and porcine sclera," J. Cataract Refract. Surg. **30**(3), 689–695 (2004).
65. M. Asejczyk-Widlicka, R. Schachar, and B. K. Pierscionek, "Optical coherence tomography measurements of the fresh porcine eye and response of the outer coats of the eye to volume increase," J. Biomed. Opt. **13**(2), 024002 (2008).
66. B. Coudrillier, J. Tian, S. Alexander, K. M. Myers, H. A. Quigley, and T. D. Nguyen, "Biomechanics of the human posterior sclera: age-and glaucoma-related changes measured using inflation testing," Invest. Ophthalmol. Vis. Sci. **53**(4), 1714–1728 (2012).

Biomedical Optics EXPRESS

67. A. Curatolo, J. Birkenfeld, E. Martínez, J. A. Germann, J. Palací, D. Pascual, G. Muralidharan, J. Solarski, K. Karnowski, and M. Wojtkowski, and others, "*Customized swept-source optical coherence tomography system for air-puff induced corneal deformation imaging on multiple meridians (Conference Presentation)*," in *Ophthalmic Technologies XXX* (2020), Vol. 11218, p. 112180 V.
68. T. W. Olsen, S. Sanderson, X. Feng, and W. C. Hubbard, "Porcine sclera: thickness and surface area," Invest. Ophthalmol. Vis. Sci. **43**, 2529–2532 (2002).
69. M. Gora, K. Karnowski, M. Szkulmowski, B. J. Kaluzny, R. Huber, A. Kowalczyk, and M. Wojtkowski, "Ultra high-speed swept source OCT imaging of the anterior segment of human eye at 200 kHz with adjustable imaging range," Opt. Express **17**(17), 14880–14894 (2009).
70. W. S. Rasband, "National Institutes of Health, Bethesda, Maryland, USA," http//imagej. nih. gov/ij/ (2011).
71. Y. Hon and A. K. C. Lam, "Corneal deformation measurement using Scheimpflug noncontact tonometry," Optom. Vis. Sci. **90**(1), e1–e8 (2013).
72. R. E. Norman, J. G. Flanagan, S. M. K. Rausch, I. A. Sigal, I. Tertinegg, A. Eilaghi, S. Portnoy, J. G. Sled, and C. R. Ethier, "Dimensions of the human sclera: thickness measurement and regional changes with axial length," Exp. Eye Res. **90**(2), 277–284 (2010).
73. L. R. Bartholomew, D. X. Pang, D. A. Sam, and J. C. Cavender, "Ultrasound biomicroscopy of globes from young adult pigs," Am. J. Vet. Res. **58**, 942–948 (1997).
74. A. Thale and B. Tillmann, "The collagen architecture of the sciera—SEM and immunohistochemical studies," Annals of Anatomy - Anatomischer Anzeiger **175**(3), 215–220 (1993).
75. B. J. Curtin, "Physiopathologic aspects of scleral stress-strain," Trans. Am. Ophthalmol. Soc. **67**, 417 (1969).
76. M. Spitznas, "The fine structure of human scleral collagen," Am. J. Ophthalmol. **71**(1), 68 (1971).
77. F. Boschetti, V. Triacca, L. Spinelli, and A. Pandolfi, "Mechanical characterization of porcine corneas," J. Biomech. Eng. **134**(3), 031003 (2012).
78. K. Yang, L. Xu, Q. Fan, D. Zhao, and S. Ren, "Repeatability and comparison of new Corvis ST parameters in normal and keratoconus eyes," Sci. Rep. **9**, 1–10 (2019).
79. M. Jkedzierowska and R. Koprowski, "Novel dynamic corneal response parameters in a practice use: a critical review," Biomed. Eng. Online **18**(1), 17 (2019).
80. R. Ambrósio Jr, F. F. Correia, B. Lopes, M. Q. Salomão, A. Luz, D. G. Dawson, A. Elsheikh, R. Vinciguerra, P. Vinciguerra, and C. J. Roberts, "Suppl-1, M2: corneal biomechanics in ectatic diseases: refractive surgery implications," Open Ophthalmol. J. **11**(1), 176–193 (2017).
81. W. Kokott, "Über mechanisch-funktionelle Strukturen des Auges," Albr. von Graefes Arch. für Ophthalmol. **138**(4), 424–485 (1938).
82. P. Fratzl, "Collagen: structure and mechanics, an introduction," in *Collagen* (Springer, 2008), pp. 1–13.
83. B. Wang, Y. Hua, B. L. Brazile, B. Yang, and I. A. Sigal, "Collagen fiber interweaving is central to sclera stiffness," Acta Biomater. **113**, 429–437 (2020).
84. Y. Zhang, Z. Li, L. Liu, X. Han, X. Zhao, and G. Mu, "Comparison of riboflavin/ultraviolet-A cross-linking in porcine, rabbit, and human sclera," Biomed Res. Int. **2014**, 194204 (2014).
85. S. Kling, H. Ginis, and S. Marcos, "Corneal biomechanical properties from two-dimensional corneal flap extensiometry: application to UV-riboflavin cross-linking," Invest. Ophthalmol. Vis. Sci. **53**(8), 5010–5015 (2012).
86. L. I. V. Lopez, D. Bronte, J. Germann, and S. Marcos, "Scleral cross-linking using Rose Bengal-Green Light," Invest. Ophthalmol. Vis. Sci. **61**, 3415 (2020).
87. R. Grytz, M. A. Fazio, M. J. A. Girard, V. Libertiaux, L. Bruno, S. Gardiner, C. A. Girkin, and J. C. Downs, "Material properties of the posterior human sclera," J. Mech. Behav. Biomed. Mater. **29**, 602–617 (2014).
88. M. Á. Ariza-Gracia, J. F. Zurita, D. P. Piñero, J. F. Rodriguez-Matas, and B. Calvo, "Coupled biomechanical response of the cornea assessed by non-contact tonometry. A simulation study," PLoS One **10**, e0121486 (2015).
89. A. Ramier, B. Tavakol, and S.-H. Yun, "Measuring mechanical wave speed, dispersion, and viscoelastic modulus of the cornea using optical coherence elastography," Opt. Express **27**(12), 16635–16649 (2019).
90. M. Singh, Z. Han, A. Nair, A. Schill, M. D. Twa, and K. V Larin, "Applanation optical coherence elastography: noncontact measurement of intraocular pressure, corneal biomechanical properties, and corneal geometry with a single instrument," J. Biomed. Opt. **22**, 20502 (2017).
91. J. Birkenfeld, J. A. Germann, A. De Castro, A. De la Hoz, A. Curatolo, and S. Marcos, "Assessment of asymmetries in biomechanical properties from corneal deformation imaging," Invest. Ophthalmol. Vis. Sci. **60**, 6809 (2019).